
Unsupervised discovery of the shared and private geometry in multi-view data

Sai Koukuntla

Department of Biomedical Engineering
Johns Hopkins University
Baltimore, MD 21218
skoukun1@jh.edu

Joshua B. Julian

Princeton Neuroscience Institute
Princeton University
Princeton, NJ 08540
jjulian@princeton.edu

Jesse C. Kaminsky

Princeton Neuroscience Institute
Princeton University
Princeton, NJ 08540
jk8386@princeton.edu

Manuel Schottdorf

Princeton Neuroscience Institute
Princeton University
Princeton, NJ 08540
ms81@princeton.edu

David W. Tank

Princeton Neuroscience Institute
Princeton University
Princeton, NJ 08540
dwtank@princeton.edu

Carlos D. Brody

Princeton Neuroscience Institute
Princeton University
Princeton, NJ 08540
brody@princeton.edu

Adam S. Charles

Department of Biomedical Engineering
Center for Imaging Science
Johns Hopkins University
Baltimore, MD 21218
adamsc@jhu.edu

Abstract

Modern applications often leverage multiple views of a subject of study. Within neuroscience, there is growing interest in large-scale simultaneous recordings across multiple brain regions. Understanding the relationship between views (e.g., the neural activity in each region recorded) can reveal fundamental principles about the characteristics of each representation and about the system. However, existing methods to characterize such relationships either lack the expressivity required to capture complex nonlinearities, describe only sources of variance that are shared between views, or discard geometric information that is crucial to interpreting the data. Here, we develop a nonlinear neural network-based method that, given paired samples of high-dimensional views, disentangles low-dimensional shared and private latent variables underlying these views while preserving intrinsic data geometry. Across multiple simulated and real datasets, we demonstrate that our method outperforms competing methods. Using simulated populations of lateral geniculate nucleus (LGN) and V1 neurons we demonstrate our model's ability to discover interpretable shared and private structure across different noise conditions. On a dataset of unrotated and corresponding but randomly rotated MNIST digits, we recover private latents for the rotated view that encode rotation angle regardless of digit class, and places the angle representation on a 1-d manifold,

while shared latents encode digit class but not rotation angle. Applying our method to simultaneous Neuropixels recordings of hippocampus and prefrontal cortex while mice run on a linear track, we discover a low-dimensional shared latent space that encodes the animal’s position. We propose our approach as a general-purpose method for finding succinct and interpretable descriptions of paired data sets in terms of disentangled shared and private latent variables.

1 Introduction

Many modern applications require the ability to identify and interpret the relationships between multiple high-dimensional datasets that represent multiple views of the same underlying system. Examples exist across applications, for example the shared semantic overlap between text captions and images; finding the underlying variables shared between counts of mRNA transcripts and protein counts [2]; and performing sensor fusion in robotics [10]. This paradigm of multi-view data is becoming increasingly important in neuroscience with the rapid growth of new recording technologies that enable recording of many neurons in multiple brain regions simultaneously [22, 40, 4]. Each brain region can be thought of as a view into the underlying brain-wide activity. We then wish to understand what information is encoded in each brain area separately and which information is shared in a joint computation. Operating on the individual brain areas’ activity is confounded by the joint, nonlinear mixing of these two information types; shared and private.

To enable a deeper understanding and interpret which computations are local and which are global, we thus need to *disentangle* these different information types. However, disentangling by itself is insufficient for understanding; assessing the intrinsic geometry of the disentangled shared and private data can provide fundamental clues towards extracting biological insight and into how the brain structures internal representations of information within and across regions. For example, work from single regions has demonstrated a ring geometry in the population activity of head direction cells, enabling blind discovery and decoding of the represented variable [5], predictions of theoretical continuous attractor models of the entorhinal cortex grid cell system have been confirmed through topological analysis of experimental data that indicated a toroidal geometry in the activity of that population of neurons [13], and geometry-preserving retinotopic maps have been used to delineate the borders of different but adjacent visual regions [9, 51]. However, extending geometry-estimation approaches to multiple regions is complicated by the fact that brain regions typically multiplex several different types of information. Estimating the geometry of the information specifically shared with another region therefore requires being able to separate the private from the shared information.

In general, learning the geometry of data has been the domain of dimensionality reduction [7, 45, 32], and more specifically manifold learning [44, 39, 36]. These methods primarily focus on quantifying the latent relationships between data points through either learning graphs on data [26, 33, 15, 26] or by estimating geodesic paths that define the manifold surface, e.g., [43, 6, 34]. These approaches effectively treat a local distance between nearby data points as a first step or as a primary quantity that is to be retained in the learned structure. Shared data manifolds in multi-view data typically extend these ideas as a “union” operator, i.e., data from both views are merged into a single manifold where local distances in each dataset for the basis for the embedding [11, 50, 35]. Unfortunately, when there is a mix of private and shared information in each view, the private information can cause significant deviations in the computed local distances, skewing any hope of embedding points with similar shared information but different private information together. This effect becomes more pronounced as the amount of private and shared information become comparable. Therefore a critical step in learning the geometry of each of the shared and private sub-manifolds is to first disentangle the shared and private information.

Thus a key requirement of this endeavor are methods that can extract from two distinct but paired datasets (\mathbf{A} and \mathbf{B}) a single shared model that captures the maximal variance jointly in both datasets and separates that shared representation from any additional information private to one dataset or another. Mathematically we can phrase this task as an inverse problem where for any sample of paired data points $\mathbf{x}_A \in \mathbf{A}$ and $\mathbf{x}_B \in \mathbf{B}$ there exist a shared set of variables \mathbf{s} and two private sets of variables \mathbf{z}_A and \mathbf{z}_B such that $\mathbf{x}_A = g_A(\mathbf{s}, \mathbf{z}_A)$ and $\mathbf{x}_B = g_B(\mathbf{s}, \mathbf{z}_B)$ for two distinct nonlinear functions $g_A(\cdot)$ and $g_B(\cdot)$, where \mathbf{z}_A , \mathbf{s} and \mathbf{z}_B are all independent of each other (i.e., "disentangled"). Our goal is to find $\{g_A(\cdot); g_B(\cdot); \mathbf{z}_A; \mathbf{s}; \mathbf{z}_B\}$.

This formulation is very general, in the sense that any joint distribution $p(\mathbf{A}, \mathbf{B})$ can be described this way. But it is also not unique: many possible forms of $\{g_A(\cdot); g_B(\cdot)\}$ and corresponding representations $\{z_A, s, z_B\}$ can be used to describe a given joint distribution $p(\mathbf{A}, \mathbf{B})$. Some of these representations will be more easily interpreted than others. Here we follow [42] in positing that representations that preserve intrinsic data geometry are likely to be more interpretable than those that don't. Unfortunately, estimating shared or private geometry in the data space is extremely difficult as any measures of distance can be skewed by the potentially nonlinear mixing between their latents. Thus estimating geometry is much more natural in the disentangled representation $\{z'_A, s', z'_B\}$. Specifically, we can seek a bijective transformation of each of these latent spaces to obtain a final representation $\{z_A, s, z_B\}$ that preserves each of their intrinsic data geometries.

Due to the importance of this task across fields, many methods have been developed to try and address the disentangling of private and shared latents. These methods either suffer from limitations in expressibility, e.g., by modeling the latent spaces as linear [21, 29, 41], imperfect separation of private and shared information, e.g., via not modeling the private latents [1, 46, 49, 23, 47], or failing to preserve intrinsic geometry [30, 48]. There thus exists a need for a robust model that can disentangle highly nonlinearly mixed shared and private information from multi-view data while preserving the data geometry.

In this work we therefore present a new model—Submanifold Partitioning via Least-variance Informed Channel Estimation (SPLICE)—that extracts the shared and private geometries, i.e., their respective submanifolds from a multi-view dataset. Our approach is based on an autoencoder with a “cross butterfly” architecture that splits the latent state into shared and private variables. Our framework simultaneously minimizes the error in recovering the data from the shared and private variables together, while minimizing the ability of each dataset’s private latent space to predict the other’s. Given this disentangled representation, our approach then leverages a cost function based geodesic distance preservation [39] that retains the submanifold structure of the private and the shared latent spaces.

The primary contributions of our work are: 1) a new network architecture (SPLICE) that separates and captures both the shared and private intrinsic geometry of two datasets, 2) validation of the architecture in controlled simulations of LGN-V1 connections 3) multiple real-data examples showing that our network can correctly separate highly nonlinear relationships in very few latent variables, and 4) comparison to the state-of-the-art methods [30, 47, 23], demonstrating superior disentangling and geometry preservation in highly nonlinear mixing conditions.

2 Related Work

Within neuroscience, significant progress in assessing the relationship between activity in different brain regions has already been achieved using models that assume either a linear link between latent variables and neural activity [38, 18, 17, 8, 12], or linear followed by a pointwise nonlinear function such as $\text{softplus}(\cdot)$ or exponential [16, 3, 24]. In terms of artificial neural networks, all of these can be thought of as having a single, potentially nonlinear, layer between latent variables and predicted neural activity. The advances in many of these studies are related to the temporal dynamics of the latent variables, an aspect not addressed here. Some of the studies explicitly distinguish latents labeled as shared versus latents labeled as private to each region. However, an important issue is that many, perhaps most, neural representations are known to be nonlinear. As a single example that we will return to below, the activity of visual neurons in the lateral geniculate nucleus (LGN) or primary visual cortex (V1) in response to a bar of light is not a linear (or monotonic, like $\text{softplus}(\cdot)$ or exponential) function of bar position. This suggests that many datasets may not be well described with linear or generalized linear approaches. Here we allow more complex nonlinear relationships by using link functions parametrized by deep neural networks.

Within machine learning, methods such as deep canonical correlation analysis (DCCA) [1] or joint embedding approaches [46] extend the classical canonical correlation analysis (CCA) to the nonlinear setting. These methods learn arbitrary functions, modeled as deep neural networks, that maximize the correlations between each view’s embedding. These methods, however, are unconstrained by reconstruction and permit trivial solutions that maximize correlation without representing significant information in the data. To solve this drawback, methods have been proposed to either append a maximum entropy cost over each view’s latents [49], or to include a reconstruction cost, instantiated

as another set of read-out neural networks in an auto-encoder type architecture [47]. These methods, however, only model the shared information. When significant private information is present in one or both views, these additional terms can lead to leakage of private information by virtue of the private information being the only way to increase the entropy or reconstruction once all the shared information has been accounted for.

More recent methods have also modeled the private latents alongside the shared. Wang 2016 take a variational autoencoder (VAE) approach to DCCA. In essence, 3 matched variational autoencoders are used to generate the three latents (one shared and two privates). The VAE structure has an isotropic Gaussian latent distributions, encouraging the latent variables to all be statistically independent both within and between sets of latents. A similar VAE-based approach of Lee and Pavlovic trains two VAEs, one for each view [28]. The resulting latents for each view are split into two (producing four total sets of latent variables) and a subset of each view’s latents are encouraged to match, creating an effective shared latent space [27]. Lyu 2021 [30] is based on AE based DCCA (e.g., Wang 2016). They learn one AE for each view, with a subset of each being the shared or private (similar to [27]). DCCA is then used to align the shared spaces of each AE output, with an adversarial cost serving to disentangle the shared and private latents. Yao 2023 demonstrated that for certain smoothness and sampling assumptions, the procedure of Lyu 2021 can identify the shared latent [49]. All these methods, while representing the current state-of-the-art have two major drawbacks: destroys geometry, leakage.

Different from the above, Mathieu et al. 2016 [31] is a semisupervised approach where pairs of data points within the same class are compared to data points across classes to identify a single encoder decoder pair. While the model is simplified by having only one encoder and decoder, and the model architecture should limit leakage of shared latents into the private, this approach is limited by the class assumptions. First, the data must fall into discrete classes, limiting utility in more continuously varying datasets, and moreover the class of each point is assumed known. Thus this approach is not directly applicable to most neural data.

The putatively private latents z_a and z_b will be truly private to A and B respectively only if they are independent from each other and from the shared latent S – that is, the latent variables must be "disentangled" [20]. We are aided in having auxiliary "region A " versus "region B " labels in the data set. And we are further aided in not seeking total disentanglement of each element within each of the latent variable vectors (for example, we do not seek to disentangle the different components within the vector z_b from each other), but only partial disentanglement (each of the overall vectors z_a , S , z_b should be independent from each other). We therefore do not use disentangling approaches that minimize Total Correlation (TC), such as [25] or [27], even while the latter study has a generative model that is very close to that used here in explicitly distinguishing private and shared latents and having a multilayer nonlinear relationship between latents and observables. Instead we use an early disentangling approach, predictability minimization [37], which scales poorly for total disentanglement but scales well for the partial disentanglement we seek here, and is straightforwardly combined with the approach, to be described below, for preserving intrinsic data geometries.

3 Submanifold Partitioning via Least-variance Informed Channel Estimation (SPLICE)

Given two views A and B , SPLICE is designed with two features in mind: First, the ability to separate the shared representation of two datasets from each set’s private representations. Second, the ability to preserve the intrinsic geometry of each representation (shared, private to A , and private to B).

3.1 Observation model

We begin with our observation model, which characterizes two sets of observable data A and B as being generated via two nonlinear functions $g_A(\cdot)$ and $g_B(\cdot)$ such that any paired sample $\mathbf{x}_A \in A \subset \mathcal{R}^{N_A}$ from dataset A and $\mathbf{x}_B \in B \subset \mathcal{R}^{N_B}$ from dataset B can be written as

$$\mathbf{x}_A = g_A(\mathbf{s}, \mathbf{z}_A), \quad \mathbf{x}_B = g_B(\mathbf{s}, \mathbf{z}_B), \quad (1)$$

where \mathbf{z}_A , \mathbf{s} , \mathbf{z}_B are all independent of each other (Fig. 1a). In these expressions $\mathbf{s} \in \mathbb{R}^{M_S}$ is a shared set of variables influencing both datasets, while $\mathbf{z}_A \in \mathbb{R}^{M_A}$ and $\mathbf{z}_B \in \mathbb{R}^{M_B}$ contribute variability to

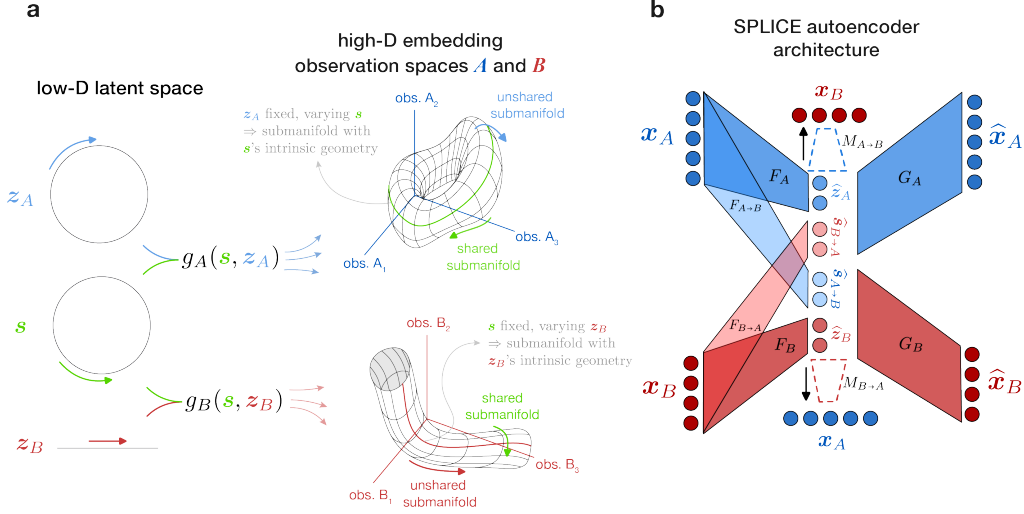


Figure 1: Problem formulation and model architecture. **a)** Illustration of the generative model. Low-dimensional private and shared latent variables are combined nonlinearly to form low-dimensional manifolds embedded in the A view and B view high-dimensional observation spaces. **b)** The SPLICE unsupervised autoencoder network architecture.

A only and B only, respectively. They are therefore private variables in the sense that, conditioned on the independence of z_A and z_B , z_B carries no information about A , and vice versa:

$$I(z_B; \mathbf{x}_A) = 0, \quad I(z_A; \mathbf{x}_B) = 0. \quad (2)$$

3.1.1 Strategies to separate the inferred shared latent variables from the private latent variables

Below, to identify these latent spaces, we will separate the inferred shared and private latents using a combination of two strategies: (1) We will guarantee that no private information can leak into the shared latents by using a "crossed butterfly" autoencoder architecture [23]. And (2) we will stop the leakage of shared information into the private latents by using predictability minimization [37] to minimize how well dataset A can be predicted from the private latents for B , and vice versa. This will minimize the information that the private latents for one view have about the other view. In other words, it will minimize the shared information in the private latents.

3.1.2 Strategy to identify and preserve the geometry of each group of latent variables

As the set of latent variables vary, they trace out low dimensional manifolds that are embedded in the high dimensional observation spaces (Fig. 1a, right). We note that if we can keep private latents separate from shared latents, then, for either of A and B , if one of its latent variables is kept fixed while the other varies, this will trace out a submanifold (of the overall data manifold) in the observation space that will have the same intrinsic geometry as that of the latent that is varying. This will be used below to assess intrinsic latent geometries from data in the observable spaces.

3.1.3 A two-step process

The second strategy requires successful separation of private and shared latents, meaning that it requires successful completion of the first strategy. Consequently, we will carry out the two strategies in sequence: first we will use an autoencoder architecture to infer latent variables that separate private from shared information. We will then employ these inferred latents to estimate the intrinsic geometries of the underlying private and shared latents. Finally, in a second training step, we will use that information to retrain our autoencoder so as to obtain an updated set of inferred latents that preserve these geometries.

3.2 Step 1. Disentangling shared from private representations

To identify the latent spaces we define an autoencoder framework, in a symmetric ‘‘crossed butterfly’’ configuration. Specifically, we define four encoders and two decoders such that each dataset generates both a shared and private set of variables, and is in turn reconstructed from a shared and private set of latents (Fig. 1b). The encoders $F_A, F_B, F_{A \rightarrow B}, F_{B \rightarrow A}$ and decoders G_A, G_B are all parameterized as multi-layer neural networks. Given an input data pair \mathbf{x}_A and \mathbf{x}_B , the estimated latents are computed as

$$\underbrace{\hat{\mathbf{z}}_A}_{\text{private A latent}} = F_A(\mathbf{x}_A), \quad \underbrace{\hat{\mathbf{z}}_B}_{\text{private B latent}} = F_B(\mathbf{x}_B), \quad \underbrace{\hat{\mathbf{s}}_{B \rightarrow A}}_{\text{shared from B latent}} = F_{B \rightarrow A}(\mathbf{x}_B), \quad \underbrace{\hat{\mathbf{s}}_{A \rightarrow B}}_{\text{shared from A latent}} = F_{A \rightarrow B}(\mathbf{x}_A) \quad (3)$$

and the reconstructed estimates of the inputs are computed as

$$\hat{\mathbf{x}}_A = G_A(\hat{\mathbf{s}}_{B \rightarrow A}, \hat{\mathbf{z}}_A), \quad \hat{\mathbf{x}}_B = G_B(\hat{\mathbf{s}}_{A \rightarrow B}, \hat{\mathbf{z}}_B). \quad (4)$$

The encoders and decoders are trained to reconstruct the inputs $(\mathbf{x}_A, \mathbf{x}_B)$ by minimizing the mean squared error between $(\hat{\mathbf{x}}_A, \hat{\mathbf{x}}_B)$ and $(\mathbf{x}_A, \mathbf{x}_B)$ (see below for loss function details). If private information about A has leaked into the putatively shared latent used to reconstruct A , optimizing the reconstruction of A can encourage keeping it there, since reconstruction encourages maximizing information about A in the latents it is reconstructed from. But the ‘‘crossed butterfly’’ configuration means that the shared latents $\hat{\mathbf{s}}_{B \rightarrow A}$ and $\hat{\mathbf{s}}_{A \rightarrow B}$ are computed from the dataset they are *not* being used to reconstruct. Consequently, they are guaranteed to carry no private information about the view they are reconstructing, and instead, by construction, can only capture information shared between the two views.

When it comes to the putatively private latents $\hat{\mathbf{z}}_A$ and $\hat{\mathbf{z}}_B$, however, the crossed butterfly architecture alone does not ensure that the $\hat{\mathbf{z}}_A$ and $\hat{\mathbf{z}}_B$ carry only private information. For this we turn to predictability minimization [37].

The central intuition in predictability minimization is that if a variable can be used to predict something about another, there must be non-zero mutual information between the two, and deep networks can be used to estimate predictability. The final two networks we use in our architecture, $M_{A \rightarrow B}$ and $M_{B \rightarrow A}$, which we term ‘‘measurement networks,’’ produce predictions of each dataset based on the putative private latent for the other:

$$\mathbf{x}_A^{\text{pred}} = M_{B \rightarrow A}(\hat{\mathbf{z}}_B), \quad \mathbf{x}_B^{\text{pred}} = M_{A \rightarrow B}(\hat{\mathbf{z}}_A). \quad (5)$$

These networks are trained to minimize the mean squared error difference between $(\mathbf{x}_A^{\text{pred}}, \mathbf{x}_B^{\text{pred}})$ and $(\mathbf{x}_A, \mathbf{x}_B)$. Note that if $I(\hat{\mathbf{z}}_B; \mathbf{x}_A) = 0$ then the output of $M_{B \rightarrow A}(\hat{\mathbf{z}}_B)$ that minimizes the squared error difference will be the mean $\bar{\mathbf{x}}_A$ of the dataset A . This is a constant with regard to the input $\hat{\mathbf{z}}_B$. Thus, with $\text{Var}[M(\cdot)]$ representing the variance in the output of a network $M(\cdot)$, for well-trained measurement networks we have

$$I(\hat{\mathbf{z}}_B; \mathbf{x}_A) = 0 \Rightarrow \text{Var}[M_{B \rightarrow A}(\hat{\mathbf{z}}_B)] = 0 \quad \text{and} \quad I(\hat{\mathbf{z}}_A; \mathbf{x}_B) = 0 \Rightarrow \text{Var}[M_{A \rightarrow B}(\hat{\mathbf{z}}_A)] = 0. \quad (6)$$

This suggests that $\text{Var}[M_{B \rightarrow A}(\hat{\mathbf{z}}_B)]$ and $\text{Var}[M_{A \rightarrow B}(\hat{\mathbf{z}}_A)]$ can be used as heuristic terms in the cost functions for the private encoders $F_B(\cdot)$ and $F_A(\cdot)$. The goal is for these terms to encourage those private encoders to produce representations $\hat{\mathbf{z}}_B$ and $\hat{\mathbf{z}}_A$ that minimize $I(\hat{\mathbf{z}}_B; \mathbf{x}_A)$ and $I(\hat{\mathbf{z}}_A; \mathbf{x}_B)$, in which case $\hat{\mathbf{z}}_B$ and $\hat{\mathbf{z}}_A$ would truly be private latents. However, $\text{Var}[M_{B \rightarrow A}(\hat{\mathbf{z}}_B)] = 0 \Rightarrow I(\hat{\mathbf{z}}_B; \mathbf{x}_A) = 0$ only for binary variables [37]. For analog variables and optimally trained, arbitrarily expressive measurement networks, minimizing their output variance will produce only the two conditions on the right of equation (7), which we refer to as ‘‘first-order independence’’:

$$\begin{aligned} \text{Var}[M_{B \rightarrow A}(\hat{\mathbf{z}}_B)] = 0 &\Rightarrow L_A(\hat{\mathbf{z}}_B) \equiv \mathbb{E}[\mathbf{x}_A | \hat{\mathbf{z}}_B] = \text{const.} \\ \text{Var}[M_{A \rightarrow B}(\hat{\mathbf{z}}_A)] = 0 &\Rightarrow L_B(\hat{\mathbf{z}}_A) \equiv \mathbb{E}[\mathbf{x}_B | \hat{\mathbf{z}}_A] = \text{const.} \end{aligned} \quad (7)$$

In other words, the functions $L_A(\hat{\mathbf{z}}_B)$ and $L_B(\hat{\mathbf{z}}_A)$ being constants imply that there is no mutual information between $\hat{\mathbf{z}}_B$ and the first moment of \mathbf{x}_A , or between $\hat{\mathbf{z}}_A$ and the first moment of \mathbf{x}_B . Note that first-order independence between \mathbf{x} and \mathbf{z} is a condition much stronger than simply decorrelation

of \mathbf{x} and \mathbf{z} , as it is a condition on the first-order moment of \mathbf{x} for each and every value of \mathbf{z} , whereas decorrelation is an average over all \mathbf{z} . For example, for a distribution composed of the data points $(z, x) = (-1, 1), (1, -1), (2, 0.5), (-2, -0.5)$, the variables x and z are uncorrelated, but x is not 1st-order independent from z .

In this terminology, N^{th} -order independence between \mathbf{x} and $\hat{\mathbf{z}}$ would be the condition $L^{(N)}(\hat{\mathbf{z}}) \equiv \mathbb{E}[\mathbf{x}^N | \hat{\mathbf{z}}] = \text{const}$. If \mathbf{x} is i^{th} -order independent from \mathbf{z} for all $i = 1 \dots N$, and $N \rightarrow \infty$, \mathbf{x} will become fully independent from \mathbf{z} , since all its moments will be independent from \mathbf{z} and therefore its distribution will be independent from \mathbf{z} . Guaranteeing first-order independence can therefore be thought of as akin to guaranteeing a first-order approximation to independence. Surprisingly, in our experiments below, we have found that first-order independence appears sufficient to lead networks towards solutions that also seem to satisfy full statistical independence (i.e., N^{th} -order independence for all N ; see Supp. Figs. 1a, 1b, 2b, 2c and see Discussion for how to check for higher order independence, and correct for it if necessary).

In summary, we aim to minimize the reconstruction loss terms \mathcal{L}_{rec}^A and \mathcal{L}_{rec}^B

$$\mathcal{L}_{rec}^A = \|\mathbf{x}_A - G_A(\hat{\mathbf{s}}_{B \rightarrow A}, \hat{\mathbf{z}}_A)\|_2^2, \quad \mathcal{L}_{rec}^B = \|\mathbf{x}_B - G_B(\hat{\mathbf{s}}_{A \rightarrow B}, \hat{\mathbf{z}}_B)\|_2^2, \quad (8)$$

while also minimizing the variance in the measurement networks' outputs. Consequently, the autoencoder networks $\theta_{ae} = \{G_A, G_B, F_A, F_B, F_{A \rightarrow B}, F_{B \rightarrow A}\}$ will be optimized according to

$$\begin{aligned} \mathcal{L}_{SPLICE} &= \mathbb{E}[\mathcal{L}_{rec}^A + \mathcal{L}_{rec}^B + \text{Var}[M_{A \rightarrow B}(\hat{\mathbf{z}}_A)] + \text{Var}[M_{B \rightarrow A}(\hat{\mathbf{z}}_B)]] \\ \theta_{ae}^* &= \arg \min_{\theta_{ae}} \mathcal{L}_{SPLICE} \end{aligned} \quad (9)$$

The loss function above depends on having the best possible set of predictors $\theta_{pred} = \{M_{A \rightarrow B}, M_{B \rightarrow A}\}$. We thus continuously update the measurement networks to minimize their prediction losses

$$\mathcal{L}_{pred}^A = \|\mathbf{x}_A - M_{B \rightarrow A}(\hat{\mathbf{z}}_B)\|_2^2 \quad \mathcal{L}_{pred}^B = \|\mathbf{x}_B - M_{A \rightarrow B}(\hat{\mathbf{z}}_A)\|_2^2. \quad (10)$$

so that

$$\theta_{pred}^* = \arg \min_{\theta_{pred}} \mathbb{E}[\mathcal{L}_{pred}^A + \mathcal{L}_{pred}^B] \quad (11)$$

Successful training will produce an autoencoder that reproduces its inputs while separating private and shared latent information.¹

SPLICE Model fitting To fit the multiple, interacting networks comprising the SPLICE model, we adopt an alternating optimization approach using backpropagation [37]. For each training iteration, we proceed in three steps (see algorithm 1). We first take a gradient step to minimize the joint reconstruction loss $\mathcal{L}_{rec} = \mathcal{L}_{rec}^A + \mathcal{L}_{rec}^B$ over all encoders and decoders. Next we take a gradient step to minimize the measurement prediction variances $\text{Var}[M_{A \rightarrow B}(\hat{\mathbf{z}}_A)]$ and $\text{Var}[M_{B \rightarrow A}(\hat{\mathbf{z}}_B)]$ over the corresponding private encoder. Finally, we take multiple gradient steps (the number is a hyperparameter) to minimize the measurement prediction losses $\mathcal{L}_{pred} = \mathcal{L}_{pred}^A + \mathcal{L}_{pred}^B$ over the measurement networks.

Taking multiple gradient steps to minimize \mathcal{L}_{pred} for each single step of the other losses ensures that the measurement networks are well-trained. Because the effectiveness of our disentangling strategy relies on the measurement networks being well-trained and able to learn complex relationships, we use measurement networks that are as wide and deep as the decoder networks, and periodically cold restart them to avoid local minima.

3.3 Step 2. Preserving intrinsic geometries.

In this second step, we find latent representations $\hat{\mathbf{z}}_A, \hat{\mathbf{s}}_{A \rightarrow B}, \hat{\mathbf{s}}_{B \rightarrow A}, \hat{\mathbf{z}}_B$ that preserve the intrinsic data geometries of the underlying private and shared latents. By this we mean that Euclidean distances

¹It has been noted [19] that training of the measurement networks is different, but closely related, to Generative Adversarial Networks (GANs): the $M(\cdot)$ network aims to improve its prediction of a data set, while the $F(\cdot)$ network that provides M 's input aims to hinder this prediction.

Algorithm 1 Training process for Step 1, separating shared and private latents

- 1: Initialize autoencoder networks $\theta_{ae} = \{G_A, G_B, F_A, F_B, F_{A \rightarrow B}, F_{B \rightarrow A}\}$
 - 2: Initialize measurement networks $M_{A \rightarrow B}$ and $M_{B \rightarrow A}$
 - 3: **repeat**
 - 4: **repeat** for 1000 iterations
 - 5: Encode inputs \mathbf{x}_A and \mathbf{x}_B to get all latents: $\widehat{\mathbf{s}}_{B \rightarrow A}$ and $\widehat{\mathbf{s}}_{A \rightarrow B}$, $\widehat{\mathbf{z}}_A$ and $\widehat{\mathbf{z}}_B$
 - 6: Decode shared and private latents to reconstruct inputs: $\widehat{\mathbf{x}}_A$ and $\widehat{\mathbf{x}}_B$
 - 7: Compute reconstruction loss \mathcal{L}_{rec}^A and \mathcal{L}_{rec}^B
 - 8: Compute $\text{Var}[M_{B \rightarrow A}(\widehat{\mathbf{z}}_B)]$ and $\text{Var}[M_{A \rightarrow B}(\widehat{\mathbf{z}}_A)]$
 - 9: Update encoder and decoder networks to minimize \mathcal{L}_{rec}^A and \mathcal{L}_{rec}^B
 - 10: Update encoder networks to minimize $\text{Var}[M_{B \rightarrow A}(\widehat{\mathbf{z}}_B)]$ and $\text{Var}[M_{A \rightarrow B}(\widehat{\mathbf{z}}_A)]$
 - 11: **repeat** for 5 iterations
 - 12: Use measurement networks to predict datasets from private latents: \mathbf{x}_A^{pred} and \mathbf{x}_B^{pred}
 - 13: Compute measurement networks' prediction loss \mathcal{L}_{pred}^A and \mathcal{L}_{pred}^B
 - 14: Update measurement networks to minimize $\mathcal{L}_{pred}^A + \mathcal{L}_{pred}^B$
 - 15: **until** end of 5 iterations
 - 16: **until** end of 1000 iterations
 - 17: reinitialize measurement networks $M_{A \rightarrow B}$ and $M_{B \rightarrow A}$
 - 18: **repeat** for 500 iterations
 - 19: Use measurement networks to predict datasets from private latents: \mathbf{x}_A^{pred} and \mathbf{x}_B^{pred}
 - 20: Compute measurement networks' prediction loss \mathcal{L}_{pred}^A and \mathcal{L}_{pred}^B
 - 21: Update measurement networks to minimize $\mathcal{L}_{pred}^A + \mathcal{L}_{pred}^B$
 - 22: **until** end of 500 iterations
 - 23: **until** convergence
-

in the inferred latent representations will approximately match the corresponding submanifold's geodesic distances. Critically, having separated private and shared latents in Step 1 allows estimating the geodesic distances for each latent group separately from the others. To do this, we first use a trained SPLICE network to trace out, in the observed data spaces, data points lying on a submanifold corresponding to each latent (Fig. 1a, right). We then follow the methods of [42] to estimate geodesic distances between pairs of points along each of those submanifolds. Finally, we retrain our SPLICE network, while incorporating a loss term that is minimized when Euclidean distances between pairs of points in the inferred latent spaces match the estimated geodesic distances for the corresponding pair of points in the observation spaces.

We note that successful completion of Step 1 implies that, in the limit of large number of training data points, for data points in the training set, the distributions of the corresponding samples of $\widehat{\mathbf{s}}_{B \rightarrow A}$ and $\widehat{\mathbf{z}}_A$ will be approximately independent of each other. This means that the reconstructed data points $\widehat{\mathbf{x}}_A = G_A(\widehat{\mathbf{s}}_{B \rightarrow A}, \widehat{\mathbf{z}}_A)$ will be distributed as the cross product of the data distribution of each of those two latents, passed through the decoder $G_A(\cdot)$. If the reconstruction loss is low, the reconstructed points $\widehat{\mathbf{x}}_A$ will lie approximately on the data manifold for \mathbf{x}_A . Importantly, it then follows that holding one of the latents fixed, while varying the other latent using values from the data distribution, and using $G_A(\cdot)$ to project these latents into the observation space, will produce points that are on the data manifold itself. Moreover, they will be constrained to be on a submanifold of the data manifold that has the intrinsic geometry of the latent that is being varied (Fig. 1a, right). We can therefore use the set of points constructed in such a manner to estimate geodesic distances along the submanifolds, and therefore gain insight into the intrinsic geometry for each of the latents.

For example, to obtain an example of the z_A submanifold, we randomly choose one of the values of $\widehat{\mathbf{s}}_{B \rightarrow A}$ in the data set, set $\widehat{\mathbf{s}}_{B \rightarrow A}^{fix}$ to that value, and compute

$$\widehat{\mathbf{x}}_A^{z_A \text{ submanifold}} = G_A\left(\widehat{\mathbf{s}}_{B \rightarrow A}^{fix}, F_A(\mathbf{x}_A)\right). \quad (12)$$

This is a reconstruction of \mathbf{x}_A while keeping $\widehat{\mathbf{s}}_{B \rightarrow A}$ fixed at a random point. (In practice, we replace each data point $\widehat{\mathbf{x}}_A^{z_A \text{ submanifold}}$ with the average of its local neighborhood to reduce noise.) We then measure geodesic distances between each pair of reconstructed points along the submanifold using the approach of [42]: a local nearest neighbor group is found for each point, and then geodesic

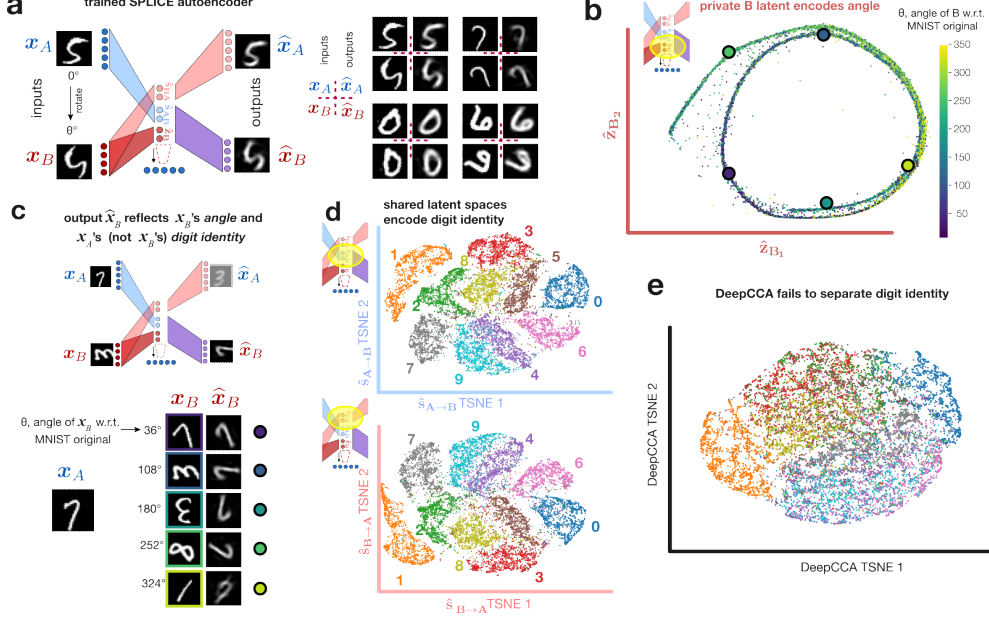


Figure 2: Rotated MNIST digits. **a)** During training, A view inputs are original MNIST digits, B view inputs are a random rotation of them. **b)** The B view private latent learns to encode the rotation angle. **c)** The $F_B(\cdot)$ private encoder distills from input x_B only rotation angle, and discards digit identity. **d,e)** TSNE clustering of the SPLICE and deepCCA shared spaces shows that SPLICE successfully separates digits into distinct clusters, whereas here dataset DeepCCA failed to do so.

distances between all pairs of points are estimated using Dijkstra’s algorithm. (In practice, we use the approach from Landmark Isomap [39], which scales better for high dimensional data.) We refer to the geodesic distances between pairs of points that are computed in this manner as D_A^{geo} . We refer to corresponding Euclidean distances in the inferred latent space \hat{z}_A as D_A^z . We then compute a loss that is the square root of the mean, over all pairs of data points, of the squared differences between D_A^z and D_A^{geo} : $\mathcal{L}_A^{geo} = \sqrt{\|D_A^z - D_A^{geo}\|_2}$. This loss will be minimized when D_A^z are the same as D_A^{geo} . We thus refer to it as a "geometry-preserving loss." A similar process is used to compute a geometry-preserving loss for each of the inferred latent spaces, $\mathcal{L}_{B \rightarrow A}^{geo}$, $\mathcal{L}_{A \rightarrow B}^{geo}$, \mathcal{L}_A^{geo} , \mathcal{L}_B^{geo} .

Finally, we retrain the SPLICE network with these loss terms added to the autoencoder loss from Equation (9), such that the optimal autoencoder parameters θ_{ae}^* become

$$\theta_{ae}^* = \arg \min_{\theta_{ae}} [\mathcal{L}_{SPLICE} + \mathcal{L}_{B \rightarrow A}^{geo} + \mathcal{L}_{A \rightarrow B}^{geo} + \mathcal{L}_A^{geo} + \mathcal{L}_B^{geo}]. \quad (13)$$

During each re-training epoch, the Euclidean distances in the latent spaces are recomputed, but the geodesic distances are computed only once before re-training begins.

4 Experiments

Experiment 1: Rotated MNIST. To investigate SPLICE’s ability to disentangle private and shared sources of variance in high-dimensional data with realistic variation, we turned to MNIST images. Dataset A consisted of the original MNIST digits and the paired dataset B consisted of a random rotation of each of A ’s digits, with the rotation angle sampled uniformly from 0 to 360 degrees (Fig. 2a). We used 60k unique images for training and 10k images for validation, with a single random rotation of each digit.

By construction, the information shared between A and B during training is the digit identity (0, 1, 2, ... etc.) and other digit-specific features (e.g. line thickness), while the information private to B is exclusively the rotation angle. Since the x_A inputs were left unrotated, there was no private information for A and we thus did not use include here a private A encoder $F_A(\cdot)$. We fit a SPLICE architecture with 30 units for each of the inferred shared latents $\hat{s}_{A \rightarrow B}$ and $\hat{s}_{B \rightarrow A}$, and 2 units for the inferred private latent \hat{z}_B , since preserving the geometry of a 1D circular variable (angle) requires two linear dimensions. Encoder, decoder, and measurement networks each consisted of 4 hidden

layers with sizes [256, 128, 64, 32]. Two features of the dataset are worth noting: First, while we expect SPLICE to identify the rotational private latent space, symmetric digits such as 0, 1, and 8, together with the indistinguishability of sixes and 180°-rotated nines, lead us to expect that the geodesic distance between angles 180° apart should not be large. Second, some MNIST digits are naturally tilted, even while all originals are labeled as being 0° w.r.t. the original.

The fit SPLICE model performed well as an autoencoder, accurately reconstructing the original and rotated digits (Fig. 2a). The inferred private latent \hat{z}_B was consistent with our expectations, with data points largely arranged along a 1D manifold (Fig. 2b). This manifold, along which rotation angle steadily increased, was approximately a double-circle, which allowed angles 180° apart to be relatively nearby in the latent space.

Remarkably, the disentangled latent space allowed us to generalize and generate arbitrarily rotated images of digits for digit-angle combinations not in the training set. Given the crossed architecture, if the private encoder $F_B(\cdot)$ truly distills only rotation angle, the reconstruction \hat{x}_B should retain input x_B 's rotation angle, but discard all of x_B 's digit-specific features, replacing them with those from input x_A . To test this, we provided different digits as inputs x_A and x_B . Indeed, the output \hat{x}_B reflected x_A 's digit identity, but with a rotation angle specified by x_B (Fig. 2c).

Both shared latent spaces $\hat{s}_{A \rightarrow B}$ and $\hat{s}_{B \rightarrow A}$ showed clear organization by digit, with clusters for similar digits (e.g. 4 and 9, 3 and 8) appearing closer together (Fig. 2d), and no apparent representation of angle (Supp. Fig. 1). By comparison, we also fit DeepCCA with 30 latent dimensions with encoders that consisted of 4 hidden layers of size [256, 128, 64, 32]. Beyond the obvious limitation of being unable to extract private information, DeepCCA failed to keep digits of different classes separated (Fig. 2e), in contrast to the clear digit clustering seen in the SPLICE shared spaces. Overall, this experiment demonstrated that, in an unsupervised manner, SPLICE can cleanly separate private and shared information across two views, and can find low-dimensional and interpretable representations of high-dimensional data.

Experiment 2: Synthetic LGN-V1 activity. Motivated by applications in neuroscience, we probed SPLICE's ability to handle nonlinear, noisy, neural-like data by simulating data representing noisy visual system responses for which ground truth information was known. Specifically, given a stimulus consisting of a bar of light presented at different positions in different trials, datasets A and B are the activity of a field of simulated LGN neurons and V1 neurons, respectively. The stimuli were kept at a single orientation (vertical). By construction, the ground truth shared information across both views is the X and Y position of the bar, which geometrically is a 2-dimensional sheet. The LGN population consisted of 400 neurons, with center-surround receptive fields whose centers were evenly spaced on a two-dimensional 20x20 grid. The V1 population consisted of two evenly spaced 20x20 grids of neurons with Gabor filter receptive fields (i.e., V1 was 800-dimensional). The first grid had vertically oriented Gabor filters and the second had horizontally oriented Gabor filters. The visual field was implemented as a 100x100 pixel grid, and the size of each neuron's receptive field was 30x30 pixels.

In addition to the shared visual stimulus, each population also responded to a private 1-D stimulus. For each population, this was generated by placing a virtual agent along a 1-D virtual linear track. Each neuron had a randomly centered Gaussian place field on this linear track. On different trials, the LGN agent and the V1 agent were placed at random, mutually independent, positions on the track. The neuronal responses to the shared and private stimuli were added linearly to obtain the final activity for each neuron. We scaled the variance of the responses to the private latents to be 6X the variance of responses to shared latents. Fig. 3a shows example stimuli and inputs to the SPLICE network in Fig. 3b show an example of the resulting LGN and V1 population activity. In some simulations, we also added i.i.d. noise to each individual neuron. For each simulation, we generated 18,900 trials, with the stimulus placed at a randomly chosen X and Y position for each trial. 80% of the trials were used for training, and the remaining 20% were used for the testing results shown in Fig. 3.

We fit SPLICE networks with different numbers of units in the latent spaces, and found that SPLICE accurately reconstructed neural activity (example reconstruction in Fig. 3b). Reduced Rank Regression (RRR) [38], a comparable but linear state-of-the-art method in neuroscience, estimates dimensionality of shared spaces by using gradually increasing dimensionality and identifying when reconstruction quality saturates. We following the same approach, and found that SPLICE correctly identified the true generative shared dimensionality ($n_s = 2$; Fig. Fig. 3c, orange). In contrast, RRR required ≈ 75 dimensions for reconstruction to saturate (Fig. 3c, blue).

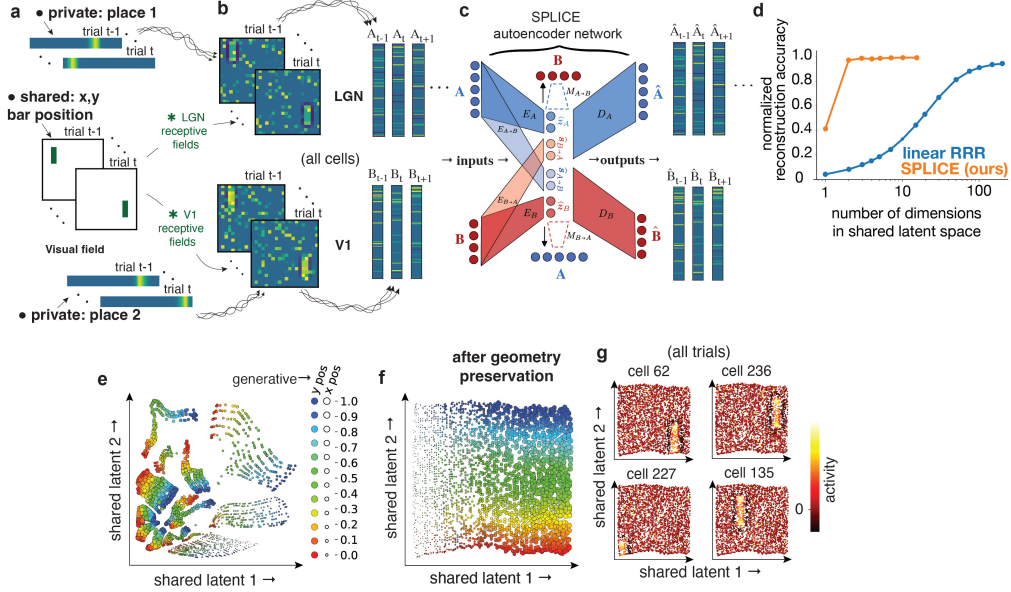


Figure 3: Simulated LGN-V1 experiments. **a**) Three independent types of data are multiplexed across two synthetic brain regions: a location on a linear track (place 1, private to region A), the x,y position of a vertical bar used as a visual stimulus (shared across regions A and B), and a second location on a second linear track (place 2, private to region B) **b**) The visual stimulus drives center-surround receptive fields, with their centers tiling the visual space in region A; region B was similar but had oriented receptive fields. For this view, the neurons have been ordered according to their visual receptive field centers. But the neurons’ private place order is unrelated to their visual field centers, so in this view the place activity appears as random noise. To maximally challenge our network we further corrupted responses with i.i.d. noise. **c**) The SPLICE network has access to neither the visual field ordering nor the place field ordering of the neurons. On each trial, it receives only a vector of activities for each region. Nearby elements in these vectors are not necessarily neurons with nearby visual or place fields. **d**) SPLICE autoencoder network. **e**) Following “RRR” (Semedo 2019), we estimate the dimensionality of the shared latents as the dimension at which the autoencoder’s reconstruction accuracy saturates. SPLICE estimates this as $d=2$, the correct ground truth. RRR, the current gold standard in systems neuroscience, severely overestimates it as $d=70$. **f**) Value of the shared latents for each trial (each dot is one trial) for the 2-d SPLICE network, before applying geometry preservation. The data structure is difficult to interpret. **g**) Same as **f**, but after applying geometry preservation. Even without having any knowledge of the existence of a visual field, geometry preservation has allowed SPLICE to arrange the data into an interpretable 2-d field. Since we know the ground truth for these synthetic data, we can label the trials by the x and y position of the visual stimulus in that trial (dot size and dot color, respectively). This shows that the axes in the estimated latent space correspond to the x - and y - axes of the visual field. **h**) Each panel shows the data as in **g**, but now colored by the activity of a randomly chosen neuron: SPLICE allows discovering that the activity coordinated across the regions has localized receptive fields that tile the shared space. **h**) SPLICE is robust to substantial noise levels. **THIS PANEL STILL TO BE ADDED**

Although the geometry-preserving step 2 did not change reconstruction quality (not shown), it had substantial impact on the geometry of the latent representations (compare Fig. 3d and e). After the geometry-preserving step 2, the data in the shared latent space were cleanly arranged in a two-dimensional sheet whose axes corresponded to the ground truth X and Y position (Fig 3e), illustrating how our unsupervised approach can generate interpretable latent geometries.

Fitting a nonlinear method, DeepCCA [1], to the same simulated data produced a shared space that distorted information about Y position and discarded most information about stimulus X position. This contrasts with SPLICE, whose reconstruction loss term requires the network to preserve shared information (such as stimulus X position) that accounts for variance in the data.

Experiment 3: Data from neurophysiological experiments.

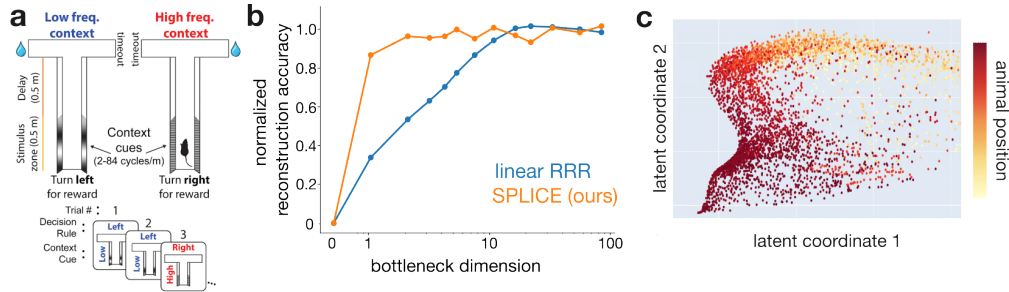


Figure 4: SPLICE and experimental neurophysiological data. **a)** On each trial, mice made a Left/Right decision on a virtual T-maze. The correct response was cued by a visual stimulus in the first half of the stem of the T. Simultaneous recordings yielded 96 neurons in hippocampus, and 348 neurons in medial prefrontal cortex. **b)** SPLICE outperformed RRR [38], summarizing the shared space in 2 dimensions, instead of 12. **c)** The shared latent space encodes the animal’s position along the maze.

Finally, we turned to experimental neurophysiological data, and asked how SPLICE would compare to state-of-the-art methods in finding and summarizing information shared across two brain regions. We fit SPLICE to electrophysiologically-recorded neural data from simultaneous Neuropixels recordings of hippocampus and prefrontal cortex, taken as mice performed a decision making task in a Virtual Reality T-maze (Fig. 4a). SPLICE outperformed Reduced Rank Regression [38] in that reconstruction quality saturated with just two dimensions, while RRR required ≈ 12 for reconstruction to saturate (Fig. 4b). The inferred latent space showed a shared encoding of the animal’s position (Fig. 4c), consistent with the presence of place cells in both brain regions. .

5 Discussion

In this work we present the SPLICE autoencoder architecture to (a) identify and disentangle shared and private low-dimensional latent spaces underlying two distinct views of the same system; (b) maximally capture variance in the data sets; and (c) find shared and private latent spaces that preserve intrinsic geometry, in the sense that Euclidean distances in the latent spaces best match geodesic distances in the intrinsic data geometry. We propose SPLICE as an approach for generating, in an unsupervised manner, succinct and interpretable summaries of complex, high-dimensional paired data sets. Our approach outperforms existing nonlinear methods such as deepCCA [1] as well as linear methods such as reduced rank regression [38].

Prior work on disentangling has focused on completely disentangling every latent variable from all others [37, 25, 27]. This modeling choice can distort geometrical shapes, for example circular latents cannot be modeled by two independent variables. Our model removes this requirement within each of the shared and private spaces to enable the learning of the data geometry in each space.

In this work we defined N^{th} -order independence such that y being N^{th} -order independent from z implies that the function $L(z)\mathbf{E}_y(y^N|z)$ is a constant. In other words, there is no mutual information between z and the N^{th} moment of y . For $N=1$ this is a much stronger condition than decorrelation, as it is a condition on the first-order moment of y for each and every value of z , whereas decorrelation is an average over all z . For example, with a distribution composed of the data points $(z, y) \in \{(-1,1), (1,-1), (2,0.5), (-2,-0.5)\}$, y and z are decorrelated, but y is not 1^{st} -order independent from z . Although stronger than decorrelation, indeed 1^{st} -order independence is not full independence. Future work can extend the SPLICE framework by constraining higher order independence, which may be required for more complex data.

The choice of basing SPLICE on an autoencoder framework rests on wanting to preserve precise geometry via the pairwise distances loss \mathcal{L}^{geo} . Alternate architectures and losses based on variational autoencoders (VAEs) may be possible, and methods exist that target independence in the latent layers of VAEs [14]. However, such models would require significant additional changes to enable the factorized posterior approximations to learn more complex geometry.

To optimize SPLICE we took a two-stage approach, first optimizing the disentangling of shared and private information and then learning each sub-manifold’s geometry. While a single end-to-end training procedure would be much more concise and aesthetic, such an approach would end up using

imperfectly disentangled data to learn the geometry, and then the resulting imperfect geometry to back propagate erroneous information into the disentangling network. We avoid this potential lack of convergence as we always want the predictor network to be maximally accurate, and so we prioritize first allowing it to train to completion before introducing the geometry piece.

Beyond the examples here where we focus on two datasets with roughly the same qualities (e.g., two images, or two populations of neurons), SPLICE has the capacity to extend further, e.g., to matching brain data with quantitative behavioral measurements from video data. Thus we believe SPLICE can be a more general purpose analysis tool across applications.

Limitations: One of the current primary limitations of SPLICE is that it can only account for two views at once. Analyzing three or more would require pair-wise runs of SPLICE on each pair of views. This limitation, while seemingly restrictive, is likewise faced by CCA, and all extensions or generalizations thereof. A second limitation of SPLICE is the omission of temporal dynamics. Splice specifically targets the geometry, and not the temporal evolution of the data. Future work should consider the power of combining these approaches. Finally, we limit SPLICE to minimizing the first-order independence. While we found this constraint computationally efficient and sufficient for our applications, new applications should check that higher-order independence holds after training SPLICE, and potentially adjust the cost function if needed.

References

- [1] Galen Andrew, Raman Arora, Jeff Bilmes, and Karen Livescu. Deep canonical correlation analysis. In Sanjoy Dasgupta and David McAllester, editors, *Proceedings of the 30th International Conference on Machine Learning*, volume 28 of *Proceedings of Machine Learning Research*, pages 1247–1255, Atlanta, Georgia, USA, 2013. PMLR.
- [2] Ricard Argelaguet, Anna SE Cuomo, Oliver Stegle, and John C Marioni. Computational principles and challenges in single-cell data integration. *Nature biotechnology*, 39(10):1202–1215, 2021.
- [3] Edoardo Balzani, Jean Paul Noel, Pedro Herrero-Vidal, Dora E Angelaki, and Cristina Savin. A probabilistic framework for task-aligned intra- and inter-area neural manifold estimation. *arXiv [q-bio.NC]*, September 2022.
- [4] K Barber, H Kim, F M Traub, B Chen, and A Vaziri. High-speed, cortex-wide volumetric recording of neuroactivity at cellular resolution using light beads microscopy. *Nature*, 2021.
- [5] Rishidev Chaudhuri, Berk Gerçek, Biraj Pandey, Adrien Peyrache, and Ila Fiete. The intrinsic attractor manifold and population dynamics of a canonical cognitive circuit across waking and sleep. *Nat. Neurosci.*, 22(9):1512–1520, September 2019.
- [6] Benjamin Culpepper and Bruno Olshausen. Learning transport operators for image manifolds. *Advances in neural information processing systems*, 22, 2009.
- [7] John P Cunningham and Zoubin Ghahramani. Linear dimensionality reduction: Survey, insights, and generalizations. *The Journal of Machine Learning Research*, 16(1):2859–2900, 2015.
- [8] Sadegh Ebrahimi, Jérôme Lecoq, Oleg Rumyantsev, Tugce Tasci, Yanping Zhang, Cristina Irimia, Jane Li, Surya Ganguli, and Mark J Schnitzer. Emergent reliability in sensory cortical coding and inter-area communication. *Nature*, 605(7911):713–721, May 2022.
- [9] S A Engel, D E Rumelhart, B A Wandell, A T Lee, G H Glover, E J Chichilnisky, and M N Shadlen. fMRI of human visual cortex. *Nature*, 369(6481):525, June 1994.
- [10] Sudeep Fadadu, Shreyash Pandey, Darshan Hegde, Yi Shi, Fang-Chieh Chou, Nemanja Djuric, and Carlos Vallespi-Gonzalez. Multi-view fusion of sensor data for improved perception and prediction in autonomous driving. In *Proceedings of the IEEE/CVF Winter Conference on Applications of Computer Vision*, pages 2349–2357, 2022.
- [11] Wenyi Feng and Zhe Wang. Multi-view multi-manifold learning with local and global structure preservation. *Applied Intelligence*, 53(10):12908–12924, 2023.
- [12] Juan A Gallego, Matthew G Perich, Raed H Chowdhury, Sara A Solla, and Lee E Miller. Long-term stability of cortical population dynamics underlying consistent behavior. *Nat. Neurosci.*, 23(2):260–270, February 2020.
- [13] Richard J Gardner, Erik Hermansen, Marius Pachitariu, Yoram Burak, Nils A Baas, Benjamin A Dunn, May-Britt Moser, and Edvard I Moser. Toroidal topology of population activity in grid cells. *Nature*, 602(7895):123–128, February 2022.
- [14] Victor Geadah, Gabriel Barello, Daniel Greenidge, Adam S Charles, and Jonathan W Pillow. Sparse-coding variational auto-encoders. *BioRxiv*, page 399246, 2018.
- [15] Scott Gigante, Adam S Charles, Smita Krishnaswamy, and Gal Mishne. Visualizing the phate of neural networks. *Advances in neural information processing systems*, 32, 2019.
- [16] Joshua Glaser, Matthew Whiteway, John P Cunningham, Liam Paninski, and Scott Linderman. Recurrent switching dynamical systems models for multiple interacting neural populations. *Adv. Neural Inf. Process. Syst.*, 33:14867–14878, 2020.
- [17] Evren Gokcen, Anna Jasper, Alison Xu, Adam Kohn, C Machens, and Byron M Yu. Uncovering motifs of concurrent signaling across multiple neuronal populations. *Adv. Neural Inf. Process. Syst.*, 2023.
- [18] Evren Gokcen, Anna I Jasper, João D Semedo, Amin Zandvakili, Adam Kohn, Christian K Machens, and Byron M Yu. Disentangling the flow of signals between populations of neurons. *Nat. Comput. Sci.*, 2(8):512–525, August 2022.
- [19] Ian Goodfellow, Jean Pouget-Abadie, Mehdi Mirza, Bing Xu, David Warde-Farley, Sherjil Ozair, Aaron Courville, and Yoshua Bengio. Generative adversarial nets. *Adv. Neural Inf. Process. Syst.*, 27, 2014.

- [20] Aapo Hyvarinen, Ilyes Khemakhem, and Hiroshi Morioka. Nonlinear independent component analysis for principled disentanglement in unsupervised deep learning. *arXiv [cs.LG]*, March 2023.
- [21] Camille Jordan. Essai sur la géométrie à n dimensions. *Bulletin de la Société Mathématique de France*, 3:103–174, 1875.
- [22] James J Jun, Nicholas A Steinmetz, Joshua H Siegle, Daniel J Denman, Marius Bauza, Brian Barbarits, Albert K Lee, Costas A Anastassiou, Alexandru Andrei, Çağatay Aydın, Mladen Barbic, Timothy J Blanche, Vincent Bonin, João Couto, Barundeb Dutta, Sergey L Gratiy, Diego A Gutnisky, Michael Häusser, Bill Karsh, Peter Ledochowitsch, Carolina Mora Lopez, Catalin Mitelut, Silke Musa, Michael Okun, Marius Pachitariu, Jan Putzeys, P Dylan Rich, Cyrille Rossant, Wei-Lung Sun, Karel Svoboda, Matteo Carandini, Kenneth D Harris, Christof Koch, John O’Keefe, and Timothy D Harris. Fully integrated silicon probes for high-density recording of neural activity. *Nature*, 551(7679):232–236, November 2017.
- [23] Paris A Karakasis and Nicholas D Sidiropoulos. Revisiting deep generalized canonical correlation analysis. *arXiv [cs.LG]*, December 2023.
- [24] Stephen L Keeley, Mikio C Aoi, Yiyi Yu, Spencer L Smith, and Jonathan W Pillow. Identifying signal and noise structure in neural population activity with gaussian process factor models. *bioRxiv*, July 2020.
- [25] Hyunjik Kim and Andriy Mnih. Disentangling by factorising. In Jennifer Dy and Andreas Krause, editors, *Proceedings of the 35th International Conference on Machine Learning*, volume 80 of *Proceedings of Machine Learning Research*, pages 2649–2658. PMLR, 2018.
- [26] Dhruv Kohli, Alexander Cloninger, and Gal Mishne. Ldle: Low distortion local eigenmaps. *Journal of machine learning research*, 22(282):1–64, 2021.
- [27] Mihee Lee and V Pavlovic. Private-shared disentangled multimodal VAE for learning of latent representations. *2021 IEEE/CVF Conference on Computer Vision and Pattern Recognition Workshops (CVPRW)*, pages 1692–1700, June 2021.
- [28] Mihee Lee and Vladimir Pavlovic. Private-shared disentangled multimodal vae for learning of latent representations. In *Proceedings of the IEEE/CVF Conference on Computer Vision and Pattern Recognition*, pages 1692–1700, 2021.
- [29] Kevin Z Lin and Nancy R Zhang. Quantifying common and distinct information in single-cell multimodal data with tilted canonical correlation analysis. *Proceedings of the National Academy of Sciences*, 120(32):e2303647120, 2023.
- [30] Qi Lyu, Xiao Fu, Weiran Wang, and Songtao Lu. Understanding latent correlation-based multi-view learning and self-supervision: An identifiability perspective. In *International Conference on Learning Representations*, 2021.
- [31] Michael F Mathieu, Junbo Jake Zhao, Junbo Zhao, Aditya Ramesh, Pablo Sprechmann, and Yann LeCun. Disentangling factors of variation in deep representation using adversarial training. *Advances in neural information processing systems*, 29, 2016.
- [32] Leland McInnes, John Healy, and James Melville. Umap: Uniform manifold approximation and projection for dimension reduction. *arXiv preprint arXiv:1802.03426*, 2018.
- [33] Kevin R Moon, David Van Dijk, Zheng Wang, Scott Gigante, Daniel B Burkhardt, William S Chen, Kristina Yim, Antonia van den Elzen, Matthew J Hirn, Ronald R Coifman, et al. Visualizing structure and transitions in high-dimensional biological data. *Nature biotechnology*, 37(12):1482–1492, 2019.
- [34] Noga Mudrik, Yenho Chen, Eva Yezerets, Christopher J Rozell, and Adam S Charles. Decomposed linear dynamical systems (dlDs) for learning the latent components of neural dynamics. *Journal of Machine Learning Research*, 25(59):1–44, 2024.
- [35] Theodoulos Rodosthenous, Vahid Shahrezaei, and Marina Evangelou. Multi-view data visualisation via manifold learning. *PeerJ Computer Science*, 10:e1993, 2024.
- [36] Sam T Roweis and Lawrence K Saul. Nonlinear dimensionality reduction by locally linear embedding. *science*, 290(5500):2323–2326, 2000.
- [37] Jürgen Schmidhuber. Learning factorial codes by predictability minimization. *Neural Comput.*, 4(6):863–879, November 1992.

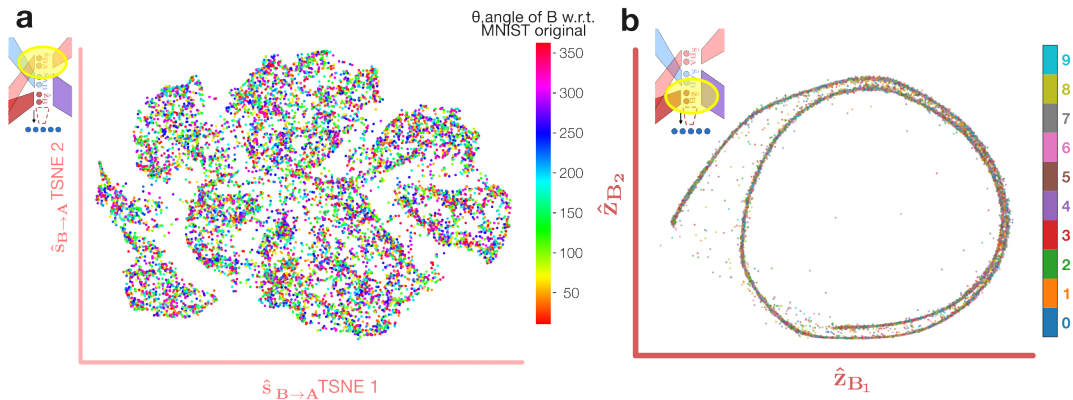
- [38] João D Semedo, Amin Zandvakili, Christian K Machens, Byron M Yu, and Adam Kohn. Cortical areas interact through a communication subspace. *Neuron*, 102(1):249–259.e4, April 2019.
- [39] V Silva and J Tenenbaum. Global versus local methods in nonlinear dimensionality reduction. *Adv. Neural Inf. Process. Syst.*, pages 705–712, 2002.
- [40] Nicholas A Steinmetz, Cagatay Aydin, Anna Lebedeva, Michael Okun, Marius Pachitariu, Marius Bauza, Maxime Beau, Jai Bhagat, Claudia Böhm, Martijn Broux, Susu Chen, Jennifer Colonell, Richard J Gardner, Bill Karsh, Fabian Kloosterman, Dimitar Kostadinov, Carolina Mora-Lopez, John O’Callaghan, Junchol Park, Jan Putzeys, Britton Sauerbrei, Rik J J van Daal, Abraham Z Vollan, Shiwei Wang, Marleen Welkenhuysen, Zhiwen Ye, Joshua T Dudman, Barundeb Dutta, Adam W Hantman, Kenneth D Harris, Albert K Lee, Edvard I Moser, John O’Keefe, Alfonso Renart, Karel Svoboda, Michael Häusser, Sebastian Haesler, Matteo Carandini, and Timothy D Harris. Neuropixels 2.0: A miniaturized high-density probe for stable, long-term brain recordings. *Science*, 372(6539), April 2021.
- [41] Nils Sturma, Chandler Squires, Mathias Drton, and Caroline Uhler. Unpaired multi-domain causal representation learning. *Advances in Neural Information Processing Systems*, 36, 2024.
- [42] J B Tenenbaum, V de Silva, and J C Langford. A global geometric framework for nonlinear dimensionality reduction. *Science*, 290(5500):2319–2323, December 2000.
- [43] Joshua Tenenbaum and William Freeman. Separating style and content. *Adv. Neural Inf. Process. Syst.*, 9, 1996.
- [44] Joshua B. Tenenbaum, Vin de Silva, and John C. Langford. A global geometric framework for nonlinear dimensionality reduction. *Science*, 290(5500):2319–2323, 2000. Publisher: American Association for the Advancement of Science.
- [45] Laurens Van der Maaten and Geoffrey Hinton. Visualizing data using t-sne. *Journal of machine learning research*, 9(11), 2008.
- [46] Guoyin Wang, Chunyuan Li, Wenlin Wang, Yizhe Zhang, Dinghan Shen, Xinyuan Zhang, Ricardo Henao, and Lawrence Carin. Joint embedding of words and labels for text classification. In Iryna Gurevych and Yusuke Miyao, editors, *Proceedings of the 56th Annual Meeting of the Association for Computational Linguistics (Volume 1: Long Papers)*, pages 2321–2331, Melbourne, Australia, July 2018. Association for Computational Linguistics.
- [47] Weiran Wang, Raman Arora, Karen Livescu, and Jeff Bilmes. On deep multi-view representation learning. In *International conference on machine learning*, pages 1083–1092. PMLR, 2015.
- [48] Weiran Wang, Xinchun Yan, Honglak Lee, and Karen Livescu. Deep variational canonical correlation analysis. *arXiv preprint arXiv:1610.03454*, 2016.
- [49] Dingling Yao, Danru Xu, Sébastien Lachapelle, Sara Magliacane, Perouz Taslakian, Georg Martius, Julius von Kügelgen, and Francesco Locatello. Multi-view causal representation learning with partial observability. *arXiv preprint arXiv:2311.04056*, 2023.
- [50] Yue Zhao, Xinge You, Shujian Yu, Chang Xu, Wei Yuan, Xiao-Yuan Jing, Taiping Zhang, and Dacheng Tao. Multi-view manifold learning with locality alignment. *Pattern Recognition*, 78:154–166, 2018.
- [51] Jun Zhuang, Lydia Ng, Derric Williams, Matthew Valley, Yang Li, Marina Garrett, and Jack Waters. An extended retinotopic map of mouse cortex. *Elife*, 6, January 2017.

A Appendix / supplemental material

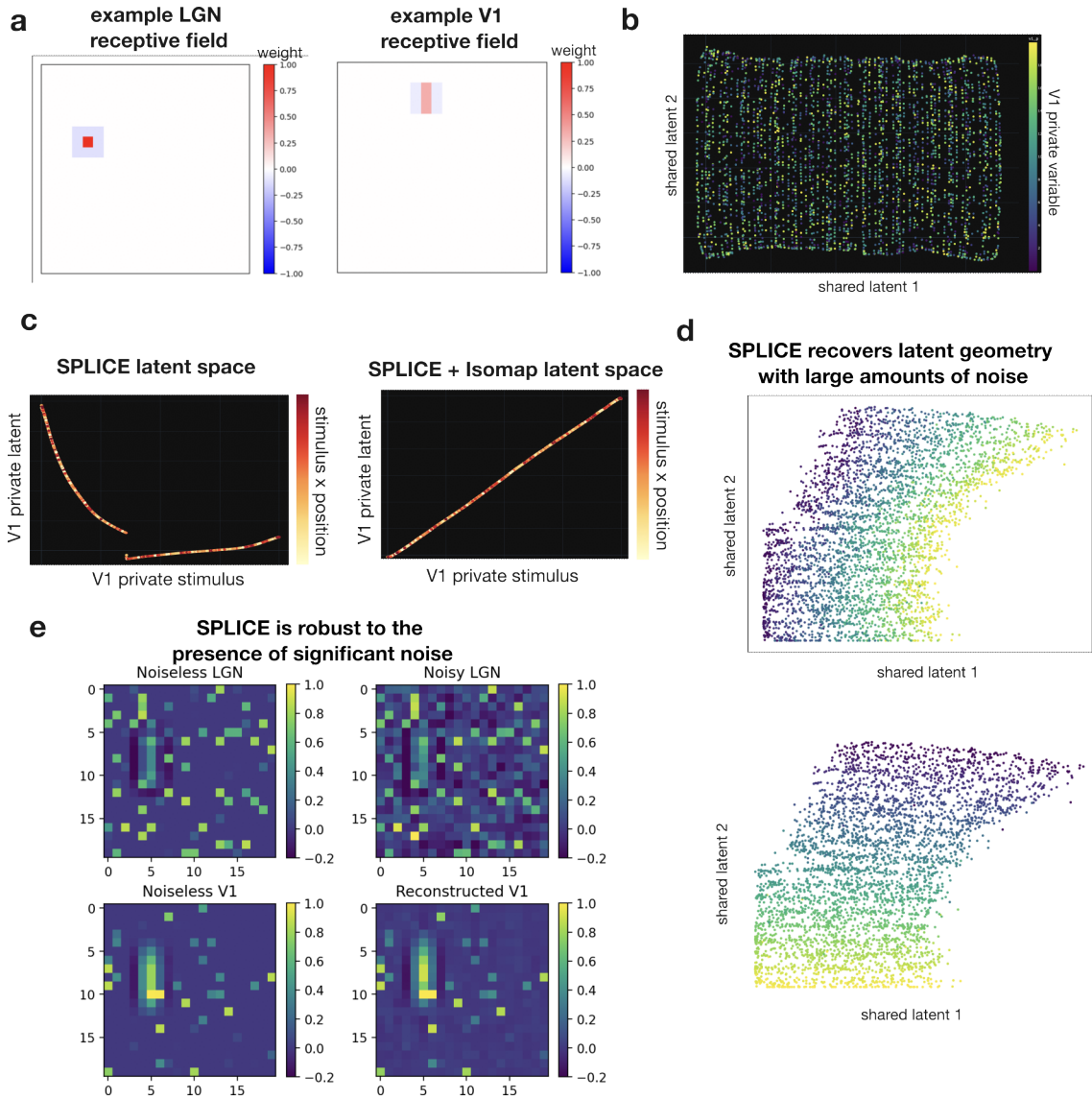
LGN-V1 Training details All encoders, decoders, and measurement networks consisted of 6 hidden layers of 200 units each. For geodesic distance calculation for all latent spaces, we averaged projections in a local neighborhood of 100 neighbors, and used 100 neighbors for the graph construction. We did not conduct a hyperparameter search, all hyperparameters described above were chosen based on intuition. All LGN-V1 models were trained on a GPU cluster using 5 RTX Quadro 5000 GPUs with 16GB of VRAM each (though the model uses much less). We did not use minibatches beyond what was required to distribute training across GPUs. To train the networks, we used the Adam optimizer with a learning rate of 0.001 that decayed linearly to 1e-5 over 25000 epochs. Results in the 3 show test set latents from a simulation that had 18,900 sample with a 80-20 train-test split.

MNIST Training details Encoders, decoders, and measurement network architectures are described above. For geodesic distance calculation in all latent spaces, we averaged projections in a local neighborhood of 20 neighbors, and used 20 neighbors for the graph construction. We did not conduct a hyperparameter search, all hyperparameters described above were chosen based on intuition. The model was trained on the same GPU cluster as the LGN-V1 models. We used minibatches of size 20. To train the networks, we used the Adam optimizer with a learning rate of 0.001 that decayed linearly to $1e-5$ over 20 epochs. 60,000 samples were used for training with 10,000 samples in the test set.

Experiment 3 Training details All encoders, decoders, and measurement networks consisted of 10 hidden layers of 100 units each. For geodesic distance calculation in all latent spaces, we did not average projections in a local neighborhood, and used 50 neighbors for the graph construction. All hyperparameters described above were chosen based on intuition. The model was trained on a single RTX 4080 GPU. To train the networks, we used the Adam optimizer with a learning rate of 0.001 that decayed linearly to $1e-5$ over 5000 epochs. The dataset consisted of 13,872 timepoints, and we used a 80-20 train-test split that respected trial structure (all time points from the same trial belonged to the same split).



Supplementary Figure 1: **a)** MNIST SPLICE shared latent space from Fig. 2d colored by angle. **b)** MNIST SPLICE private latent space from Fig. 2b colored by digit class.



Supplementary Figure 2: **a)** Example receptive fields to shared stimulus for LGN and V1 simulated neurons. **b)** LGN-V1 SPLICE shared latent space from Fig. 3e, colored by V1 private stimulus. **c)** Private latent spaces corresponding to Fig. 3d and 3e, colored by shared stimulus x position. **d)** Inferred shared latent spaces for SPLICE fit to LGN-V1 simulation with IID Gaussian noise (Norm of noise = $0.4 * \text{norm of noiseless simulation}$). Colored by stimulus x position (top) and stimulus y position (bottom) **e)** Example noiseless, input, and reconstructions for noisy simulation from **d)**